Strathprints Institutional Repository

CrossMark

ORIGINAL PAPER

Impact Angle Effects on Erosion Maps of GFRP: Applications to Tidal Turbines

Rafee Abdulmajeed Rafee Ahamed[1] · **Cameron M. Johnstone**[1] · **Margaret M. Stack**[1]

Abstract Tribology in marine renewable technologies has become of increasing interest due to the implications for developing improved materials for tidal and wave energy conversion devices. This on-going research mainly focuses on tidal devices; the materials of interest are primarily polymer-based composite materials that are used to provide structural integrity while reducing weight. These are specifically applied to turbine blades to withstand the high impact loadings in seawater conditions. At present, current materials in test trials have demonstrated some limitations in service. In this paper, some advanced experimental research has been carried out to investigate the tribological mechanisms of potential candidate composite materials to be used in tidal turbines by firstly considering the effects of various erosion parameters on the degradation modes, with and without particles in still and seawater conditions. The erosion mechanisms of composite materials used in tidal turbine blades have been evaluated using Scanning Electron Microscopy techniques to analyse the surface morphologies following testing in water representative of the constituents of coastal seawater. Generic erosion maps and the mechanistic maps have been constructed as a key to identify regions of minimum erosion for the operating conditions and to identify the significant effect of the seawater environment on the degradation of the composite. This research outcome will further help us to deeply understand and identify the erosion rates at different impact velocities and angles.

Keywords G-10 GFRP composite · Tidal turbine blades · Composite blade degradation · Solid particle erosion · Erosion rate · Particle velocity · Impingement angle · Scanning electron microscopy (SEM)

1 Introduction

Converting the energy produced from tidal flows to an economic source of electric power has many challenges, particularly in the area of reducing device mass and capital investment. Increased use of composite materials has the potential to contribute to these goals; however, a challenge exists in the production of materials sufficiently robust to withstand the environmental in-sea conditions of the exposure conditions [1]. Typically, G-10 grade, glass fibre-reinforced composite laminates are widely used as structural materials in various components and find applications in the area of precision mechanical parts, pipelines and high-voltage insulations [2]. Due to the favourable mechanical properties, composites are broadly used in the engineering industries such as marine, energy, automobile, mechanical and aerospace applications [3]. The polymer composites involved in marine applications are often exposed to challenging environments in which they experience solid particle erosion. However, the erosion behaviour in extreme marine conditions is not well understood or established, and this includes the ability of the leading edges of tidal turbine blades to withstand the exposure conditions, where the water density is approaching three

✉ Rafee Abdulmajeed Rafee Ahamed
  rafee.rafee-ahamed@strath.ac.uk

  Cameron M. Johnstone
  cameron.johnstone@strath.ac.uk

  Margaret M. Stack
  margaret.stack@strath.ac.uk

[1] Department of Mechanical and Aerospace Engineering, University of Strathclyde, James Weir Building, 75 Montrose Street, Glasgow G1 1XJ, UK

orders (784) of magnitude greater than such materials exposed to air, i.e. as in the case of composite material used for wind turbine applications [4, 5].

G-10 composites are extensively used in the high humidity applications, electrical and electronic test equipments, and electric rotor insulation. It is also widely recognized that polymers and their composites are limited in conditions where particulate erosion is an issue [4, 6]. However, the performance of these classes of materials in slurry environments, i.e. particles entrained in aqueous media, is less clear, with very few studies to date in the literature [7, 8].

This paper investigates the erosion behaviour of G-10 grade fibre-reinforced composite laminates as used in tidal turbine blades and proposes the development of erosion maps to predict and understand the erosion rate based on conditions representative of the constituents of coastal waters. Following a review of the constituents of UK coastal waters, the erosion experiments have been carried out using irregular silica sand (SiC) particles (300–150 μm) as a erodent. The erosion losses were evaluated at various impingement angles (15°–90°) representative of the range of angle of impingement experienced by tidal turbine blades and with the change of impact velocity (2.5–6.5 ms^{-1}) reflecting typical velocities experienced at the leading edge of the blade. The morphology of the eroded samples was observed using scanning electron microscopy (SEM), and the resulting damage mechanisms are discussed.

2 Experimental Investigation

2.1 Materials

The material used in the erosion test is a commercially available G.10-grade glass fibre-reinforced composite laminate material supplied by the Attwater & sons Ltd and Custom Composites Ltd. The properties of SRBG composites are given in Table 1. Rectangular specimens, with dimensions of 36 mm × 25 mm × 6 mm, were tooled and tested.

2.2 Experimental Setup and Procedure

A schematic diagram of the slurry impingement jet rig is shown in Fig. 1. The rig is equipped with a 'T'-shaped ejector, and it controls the erosion parameters by setting up the ratio of inlet nozzle to the outlet nozzle diameter (d/D), and the L-distance [9]. The erosion test was performed at three different impact velocities of 2.5, 4.5 and 6.5 ms^{-1}, and the corresponding combinations of inlet and outlet nozzles are 2.8 and 6.52 mm (2.5 ms^{-1}), 3.6 and 6 mm (4.5 ms^{-1}), and 3.6 and 4.48 mm (6.5 ms^{-1}). The impingement angle was adjusted in the range of 15°–90°. The slurry mixture consists of 3.5 % of the salt and 3 % of irregular silica sand as an erodent (Table 2). The silica sand particles were supplied by the Fife Silica Sands Ltd. The samples were tested one at a time by fixing onto the specimen holder and eroding for 30 min (Fig. 2).

2.3 Erosion Testing

The specimens were shaped and sized using the Sic paper grit 220, then cleaned with methanol and weighed using an electronic balance. In order to maintain the consistency of the erosion testing, and to avoid the particle degradation, the slurry chamber was completely cleaned, and the erodent particles were dried blasting hot air and sieved to separate the degraded particle due to the recirculation process. The experiments were performed at ambient temperature, and irregular silica sand particles in Fig. 3a, b with the size of 300–150 μm and 600–300 μm is used as an erodent. Table 3 lists the test parameters. The particle was driven by a static pressure of 0.5–1 bar, and the specimens were approximately cut into 36 mm × 25 mm × 6 mm in dimensions [11]. They were then mounted onto the specimen holder, which, fitted with an impact angle gauge, can be rotated about its vertical axis to represent the angle of attack the blade makes with the water, along the span. This

Table 1 Properties of G10 specification [10]

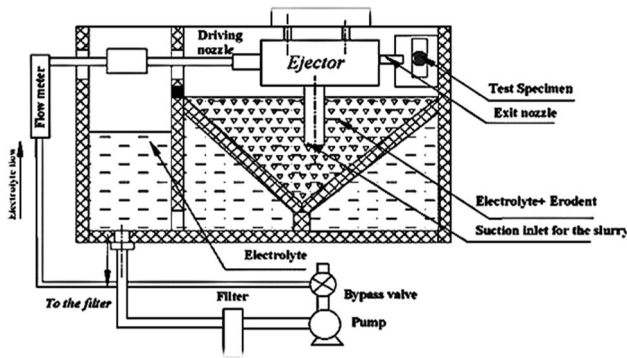| G10 sample properties	
Flexural strength (MPa)	482
Tensile strength (MPa)	320
Shear strength (MPa)	131
Density (kg/m^3)	2000
Specific gravity	1.82
Water absorption (mg)	0.8
Body colour	Green
Standard deviation (GPa) modulus	$x - 1 = 1.26, y - 1 = 0.89, z - 1 = 0.87$
Standard deviation (MPa) peak stress	$x - 1 = 4, y - 1 = 5, z - 1 = 7$

Fig. 1 Schematic diagram of slurry impingement jet rig

Table 2 Chemical composition of the sand particle [12]

SiO$_2$	Fe$_2$O$_3$	Al$_2$O$_3$	K$_2$O	CaO	Na$_2$O	LOI
98.88	0.031	0.50	0.29	<0.035	<0.02	0.22

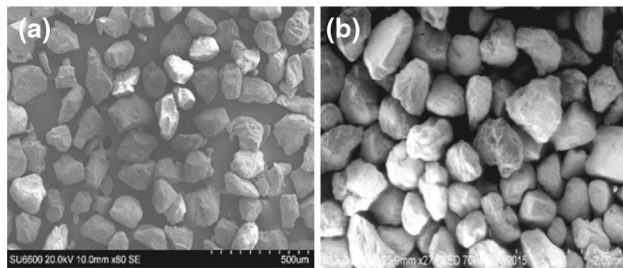Fig. 2 Rectangular specimen (36 mm × 25 mm × 6 mm)

Fig. 3 SEM analysis of SiC particles **a** 300–150 μm and **b** 600–300 μm

was eroded for 30 min with the range of angles tested from 15°–90°, representative of the typical angle of attack through to stall conditions of a stationary blade in the flow. Wear was measured by weight loss after 30 min of erosion. In order to understand the mechanism of material removal and to characterize the morphology of the eroded surfaces, the samples were analysed using scanning electron microscope (SEM). In the analysis, all samples were sputter coated with gold before the examination, and in

Table 3 Test parameters

Impact angle	15°, 30°, 45°, 60°, 75°, 90°
Solutions	Salt only, and salt + sand
Salinity (wt%)	3.5
Sand concentration (wt%)	3 (Slurry Chamber)
Test duration (min)	30
Sand particle size (μm)	300–150, 600–300
Impact velocity (ms^{-1})	2.5, 4.5, 6.5

these experiments, the charge accumulation on the samples was prevented by application of carbon gum to the edge of the sample.

3 Results

3.1 Mass Difference Under Two Various Environments

Figures 4, 5 and 6 display the influence of various environments, the impact angle and the impact velocity on the mass difference of the test samples. The test samples from the seawater condition have gained weight, whereas the samples in the test slurry achieved a dramatic mass loss. All the test samples weighed within an accuracy of 10^{-4} g. It is apparent that from the test results that intermediate impact angles have a marked more interaction with the slurry solution and the particles. This is discussed in detail under the effect of impingement angle section below.

3.2 SEM Micrographs

In order to understand the observations from the test, SEM observations were made. The images were taken using both Field Emission Electron Microscope (Hitachi SU-6600) and Tungsten Filaments Scanning Electron Microscope (Hitachi S-3700). The elemental analyses of the materials
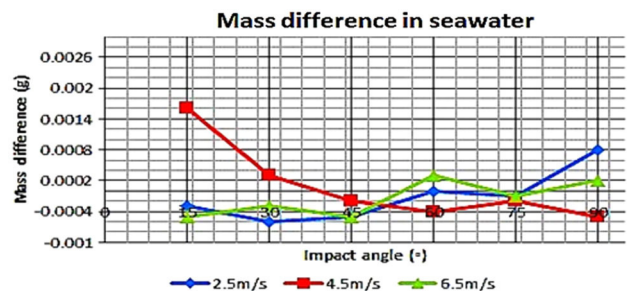

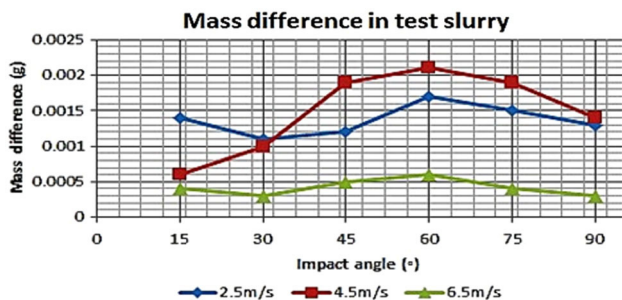Fig. 4 Mass difference as a function of impact angle in seawater

Fig. 5 Mass difference as a function of impact angle in test slurry 300–150 μm
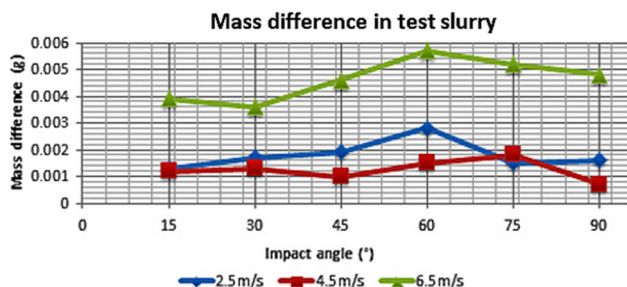

Fig. 6 Mass difference as a function of impact angle in test slurry 600–300 μm

(EDS) have been taken using an S-3700 (Hitachi) SEM (Table 4).

Figure 7a clearly indicates the deposition of salt on the surface of the test sample, whereas Fig. 7b shows the initial formation of indentations/cracks, and Fig. 7c shows platelet with fibre fragmentation along with the major indentation. All three surfaces were eroded in the speed of 2.5 ms^{-1} at 60°. This phenomenon was observed on the other samples tested in the seawater condition with different impact velocities. The impact velocity is the key factor, and it heavily influences the crystal deposition on the surface. Figure 8 justifies the above phenomenon and clearly indicates the salt crystals dried on the surface of the samples and suggests that it increases with the impact velocity. In order to support the evidence, Table 3 accounted the percentage of the salt deposited on the surface of the sample, and it is noted that 5.98 g of sodium and 6.84 g of chloride are present on the surface. There was no

Table 4 Elemental analysis

Spectrum 1	Spectrum 2	Spectrum 3
Na Cl	Na Cl	Na Cl
5.98 %, 6.84 %	5.98 %, 6.84 %	5.98 %, 6.84 %

indication for the presence of erosion under this condition on any of the samples.

Further research to understand the solid particle erosion on the test samples was undertaken through testing at multiple impact velocities and impact angles. Figure 9 indicates the surface morphologies of the eroded samples at two different impact velocities for the fixed impact angle of 60°. On magnifying the samples, Fig. 9a, b clearly shows the formation of a large crater-shaped cavity, and a multiple indentation marks associated with some linear scratches. These phenomena were consistent with other samples under similar conditions. Further results with different impact angles show different mechanisms of erosion. Figure 10a shows a significant extruded region on the surface, whereas Fig. 10b shows an extended platelet formation. Figure 11a demonstrates a significant amount of lateral cracking and the presence of fragmented silica particle scattered over the eroded surface (Fig. 11b). The formation of a large crater is possibly associated with fibre fragmentation. Figure 12a shows the formation of fibre fracture along with some evidence of minor indentations. Figure 12b indicates platelet-like morphologies with fibre fragmentation over the eroded surface.

3.3 Elevated Test Results from the Test Slurry 600–300 μm

Here we examine the increase in erosion with the different test slurry comprising 600–330 μm of SiC with seawater.

Further research to understand the solid particle erosion on the test samples was undertaken through testing at multiple impact velocities and impact angles. Figure 13 indicates the surface morphologies of the eroded samples at two different impact velocities for the fixed impact angle of 60°. On magnifying the samples, Fig. 13a, b clearly shows the formation of a large crater-shaped cavity, and a multiple indentation marks associated with some linear cracks. These phenomena were consistent with other samples under similar conditions. Further results with different impact angles show different mechanisms of erosion. Figure 14a shows significant crystal deposition on the surface, whereas Fig. 14b shows an extended dent formation. Figure 15a demonstrates a significant amount of lateral cracking and the presence of fragmented silica particle scattered over the eroded surface, Fig. 15b. The formation of a large crater is possibly associated with fibre fragmentation. Figure 16a shows the formation of fibre fracture along with some evidence of minor indentations. Figure 16b indicates platelet-like morphologies with fibre fragmentation over the eroded surface.

Fig. 7 a A close image of a surface in seawater at 60°. **b** A close view of a surface in test slurry (1) at 60°. **c** A close view of a surface in test slurry (2) at 60°
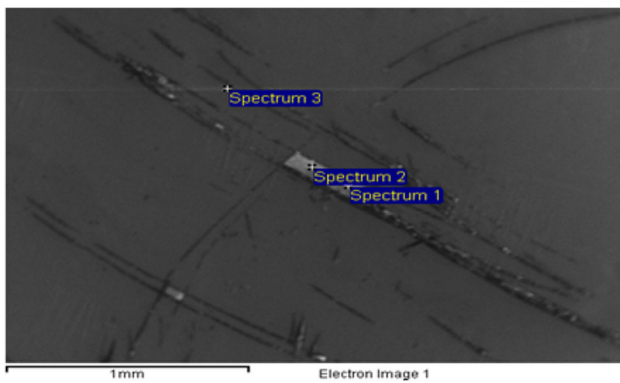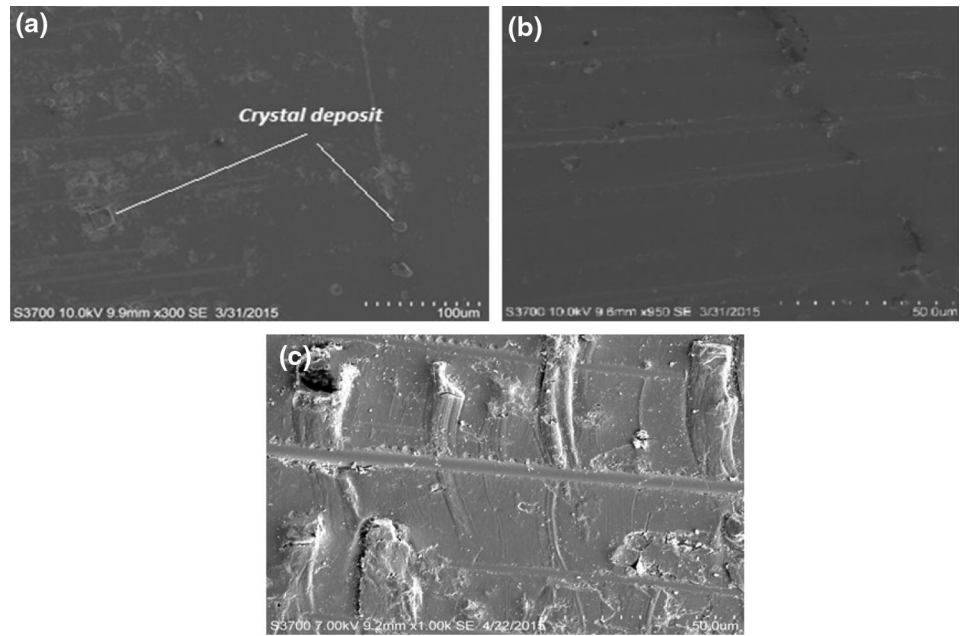

Fig. 8 SEM surface image of the eroded sample under seawater condition at 60°

4 Discussion

4.1 Effect of Impingement Angle

Angle of impingement is usually defined as the angle between the trajectory of the solid particle and the specimen surface [13] and therefore typically the angle of attack of the blade through the water. It is a widely studied and important parameter in the erosion study of materials [9]. Figures 4, 5 and 6 show mass loss as a function of impact angle for three different speeds under three conditions. The result shown in Fig. 3 indicates that the test samples seem to gain weight at certain angles and varies accordingly.
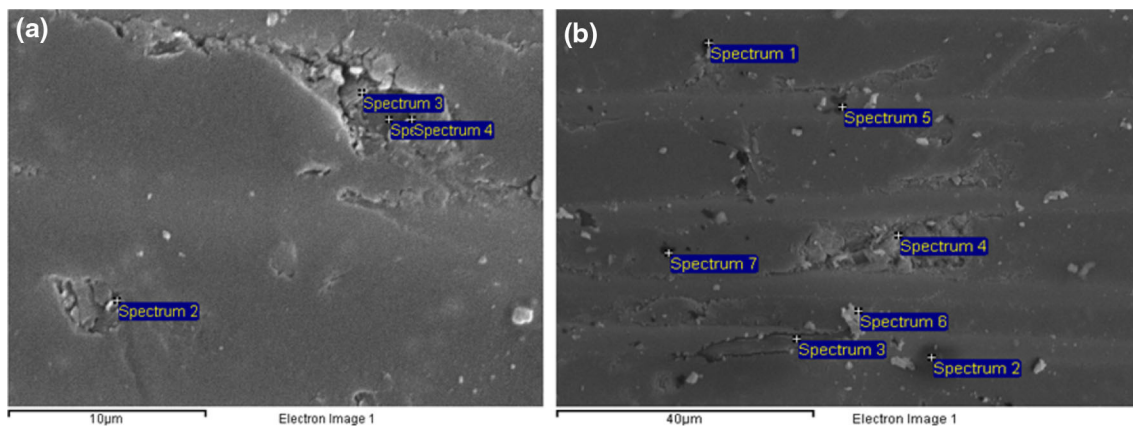

Fig. 9 SEM surface images of eroded **a** 6.5 ms^{-1}, **b** 4.5 ms^{-1} at impingement angle 60°
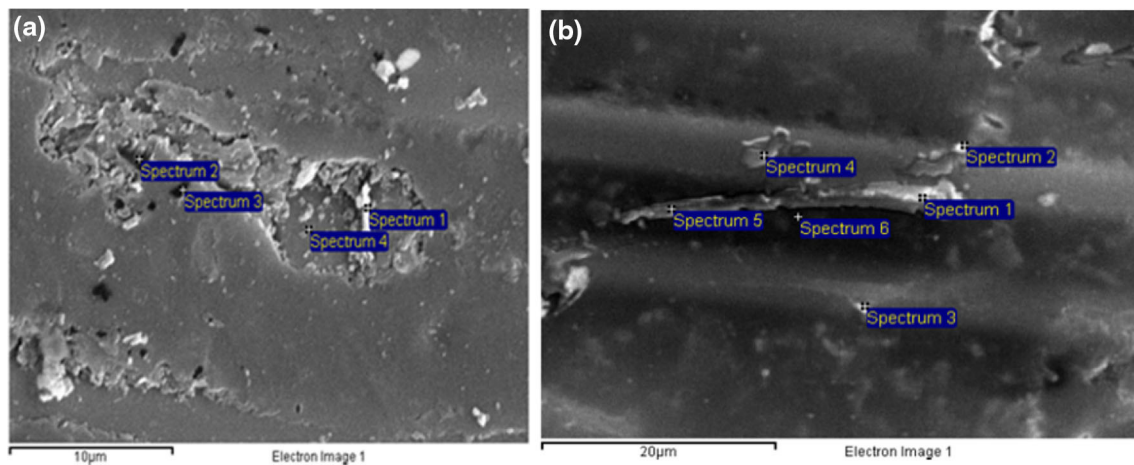
Fig. 10 SEM surface images of eroded **a** 6.5 ms^{-1}, **b** 4.5 ms^{-1} at impingement angle 45°
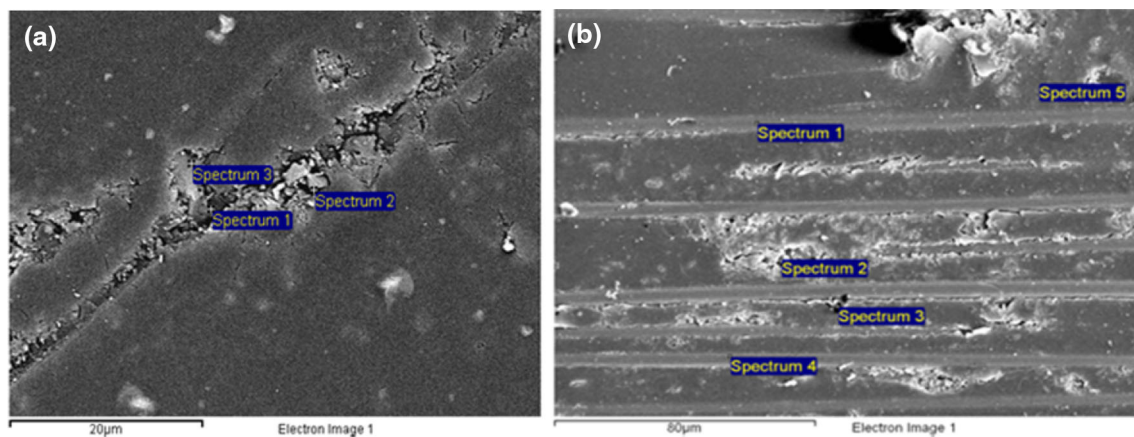

Fig. 11 SEM surface images of eroded **a** 6.5 ms^{-1}, **b** 4.5 ms^{-1} at impingement angles 75° and 15°
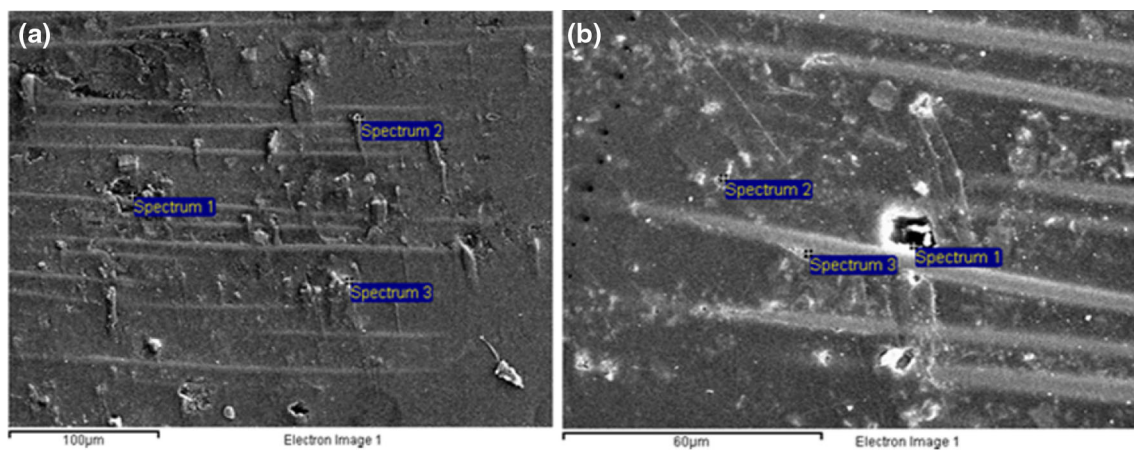

Fig. 12 SEM surface images of eroded **a** 6.5 ms^{-1}, **b** 4.5 ms^{-1} at impingement angles 30° and 90°

Figures 5 and 6 indicate that there is a significant amount of mass loss. Increases in impact velocity dramatically increase the mass loss. For example, the mass loss is found to attain a peak at 4.5 ms^{-1} (0.21 g) at 60°. The change of environment has a significant impact; factors such as erodent particle, impact angle and the impact velocity increase
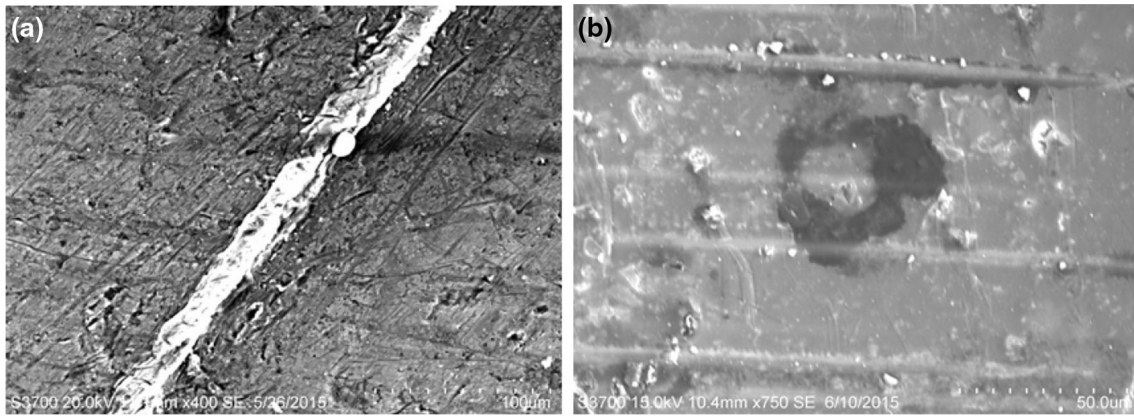
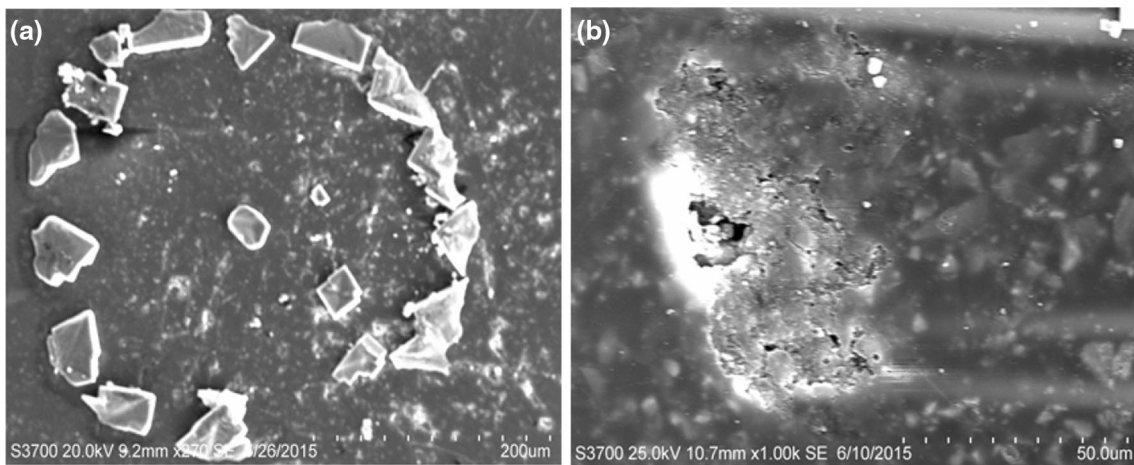**Fig. 13** SEM surface images of eroded **a** 4.5 ms^{-1}, **b** 6.5 ms^{-1} at impingement angle 60°

Fig. 14 SEM surface images of eroded **a** 4.5 ms^{-1}, **b** 6.5 ms^{-1} at impingement angle 45°

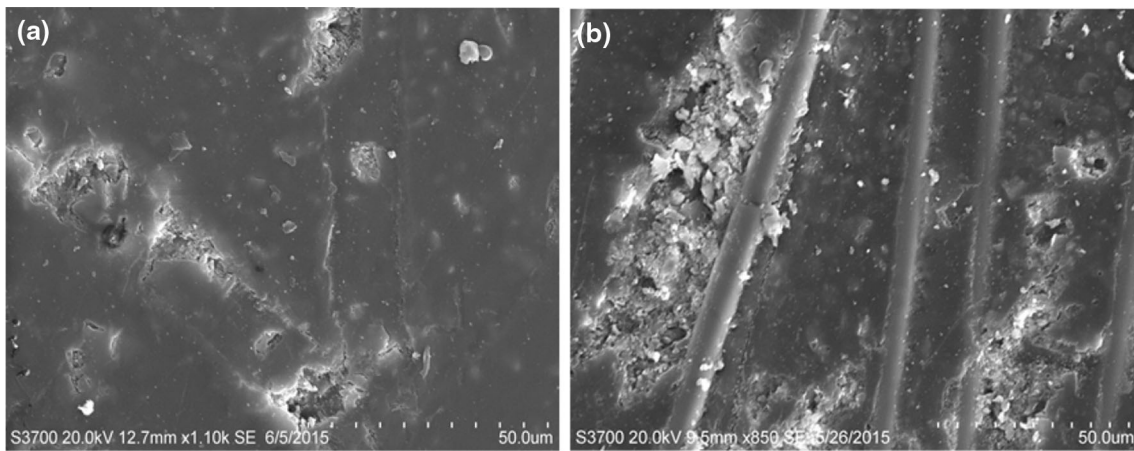**Fig. 15** SEM surface images of eroded **a** 6.5 ms^{-1}, **b** 4.5 ms^{-1} at impingement angles 75° and 15°

the mass loss, attaining a peak at intermediate impact angles [14, 15]. The reduction of the mass change at higher velocities, i.e. 6.5 ms^{-1}, may be due to frictional heating leading to a more ductile response to the erosion impacts and to the absorption of more salt on the composite at the higher velocities [16].
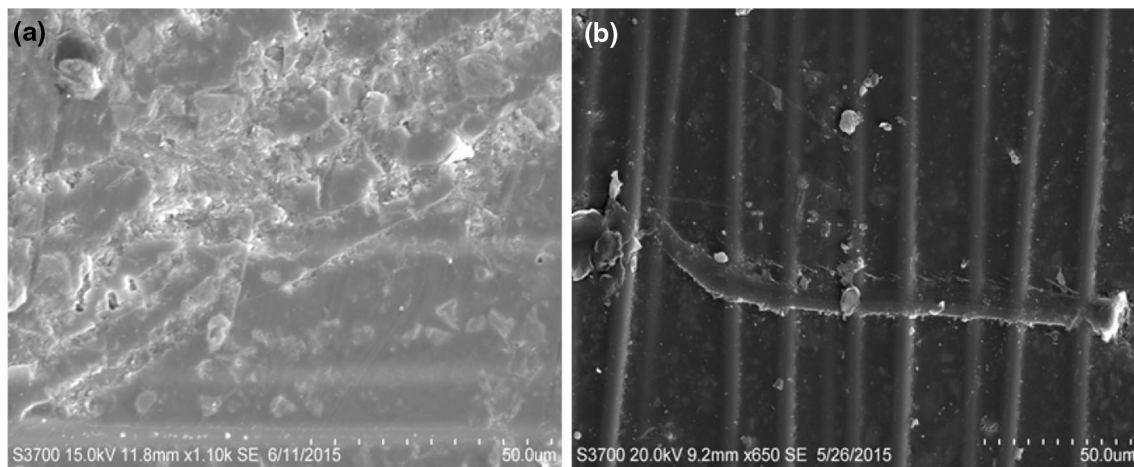
Fig. 16 SEM surface images of eroded **a** 6.5 ms^{-1}, **b** 4.5 ms^{-1} at impingement angles 30° and 90°

The combined effect of the impact velocity and the impact angle of the particles are clear in Figs. 4, 5 and 6; other parameters such as hardness of the erodent particle, their distribution and the exposure time should be considered. Previous studies on the behaviour of GFRP materials indicate that so-called "ductile" and "brittle" erosion behaviour of the test samples is generally observed at an acute angle (15°–30°) and (90°) [15, 17].

4.2 Morphology of the Eroded Surfaces

Studies on the solid particle erosion of materials clearly distinguish the difference between two erosion modes which are often seen in the literature: brittle and ductile erosion [16]. "Ductile" erosion describes material removal due to cutting and ploughing, while "brittle" erosion involves material removal due to the formation of cracks. Generally, for polymer composite materials, with a combination of ductile matrix and brittle reinforcement, behaviour intermediate between these modes is observed in the literature, depending on the fabrication process, the properties of the composite and the erosion footprint defined by the erosivity of the impacting particles [7, 18]. As it is shown in Fig. 17, the semi-ductile erosion behaviour of GFRP was also reported by Patnaik et al. [18] in which the maximum erosion appeared at 60° at various fibre volume fractions. This indicates that achieving the maximum erosion rate in the range of 45°–60° is not unexpected, and the results above are consistent with such observations.

The surface morphology of eroded surfaces indicates the modes of erosive wear occurred on the surface of the test samples. Hence, SEM studies are used to determine the wear mechanism at 15°–90° impingement angles. Figure 9a, b shows the micrographs of eroded surfaces at two different speeds (6.5 and 4.5 ms^{-1}) at fixed 60°
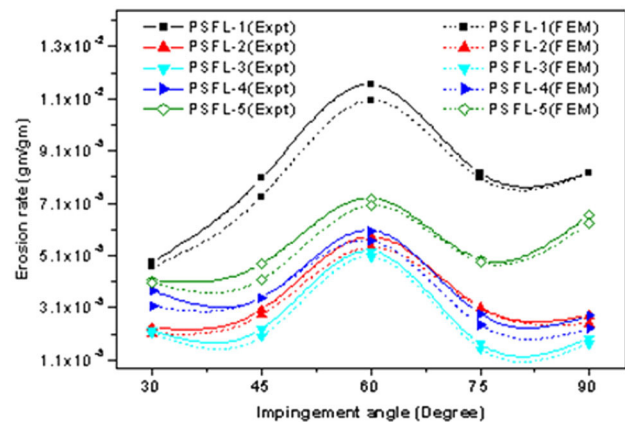

Fig. 17 Semi-ductile erosion behaviour [18]

impingement angles. It is evident from the micrograph that the material removal in the composite is dominated by the formation of a large crater-shaped cavity, and multiple indentations associated with some linear scratches. A similar effect was observed in the samples tested at the 2.5 ms^{-1} impact velocity. Figure 10a, b demonstrates the micrographs at 45° impingement angle at 6.5 and 4.5 ms^{-1} impact velocities; the process of material removal gradually starts increasing at 45°, and it reaches the peak at 60° impingement angle, whereupon the test samples experience significant erosion penetration. In order to understand the transitions at lower impact angles, i.e. between the (15°–30°), Fig. 11a shows the formation of fibre exposure along with moderate indentation over the entire surface, with Fig. 12b indicating evidence of fibre fragmentation over the eroded surfaces, with the absence of formation of deeper cracks on the composite surface. Therefore, for the conditions above, the reinforced composites exhibit a semi-

ductile behaviour having the maximum erosion rate in the range of 45°–60° [19].

In order to understand the surface behaviour of the G.10-grade glass fibre-reinforced composite laminate material, the reference material has been tested under different test slurries combining seawater and 600–300 μm SiC mixtures. The surface morphology of eroded surface indicates modes of erosive wear occurred on the surface of the test samples. Hence, SEM studies are used to determine the wear mechanism at 15°–90° impingement angles under test slurry 2. Figure 13a, b shows the micrographs of eroded surfaces at two different speeds (6.5 and 4.5 ms^{-1}) at fixed 60° impingement angle. It is evident from the micrograph that the material removal in the composite is dominated by the formation of a large crater-shaped cavity, and a multiple indentation marks associated with some linear cracks. A similar effect was observed in the samples tested at the 2.5 ms^{-1} impact velocity with the crystals being deposited over the surface. Figure 14a, b demonstrates the micrographs at 45° impingement angle at 6.5 and 4.5 ms^{-1} impact velocities; the process of material removal gradually starts increasing at 45°, and it reaches the peak at 60° impingement angle, whereupon the test samples experience significant erosion penetration. In order to understand the transitions at lower impact angles, i.e. between 15° and 30°, Fig. 15a, b indicates evidences of lateral cracking and the presence of fragmented silica particle scattered over the eroded surface. Figure 16a, b shows the formation of fibre fracture along with some evidence of minor indentations and also platelet-like morphologies with fibre fragmentation over the eroded surface. Therefore, for the conditions above, the reinforced composites exhibit a semi-ductile behaviour having the maximum erosion rate in the range of 45°–60° [19].

It should be noted that the potential consequences of the surface degradation above will lead to considerable roughness of the blade surface, impacting on the tidal flow over the blade. Propagation of this roughness will induce turbulence in the flow over the blade surface resulting in detachment of the flow from the blade surface. The Cl and Cd characteristics of the blade will reduce and increase, respectively, resulting in premature stalling of the blade during its range of operating conditions [20]. Hence, the blade operational performance will be compromised together with the power capture efficiency of the blade. Continued operation in these conditions will induce premature blade failure. Hence, the erosion studies above identify the possible reasons why composite materials developed to date pose limitations in service.

4.3 Wear Mode Regimes and Maps

Wear maps indicate mechanistic changes on the degraded surfaces of the test samples over a range of operating conditions [21]. The construction of wear mode maps assists in understanding and identifying the mechanisms involved in the material degradation and the chemical effects involved in the surface. Wear mode maps highlight the wastage rates and indicate the potential safe operation conditions for the material chosen [22]. Figure 18 shows the wear mode maps for two different conditions. The wear modes are classified into five distinct regimes: (a) low/mass gain, (b) low, (c) medium, (d) high and (e) severe. The wear mode boundary limits are as follows:

(a)   Very low/mass gain $\leq$ 8.55 μg,
(b)   8.55 μg < low $\leq$ 19.95 μg,
(c)   19.95 μg < medium $\leq$ 37.05 μg,
(d)   37.05 μg < high $\leq$ 48.45 μg and
(e)   48.45 μg < severe $\leq$ 57 μg.

Figure 19 maps the wear mode regimes for the three different conditions, and they are seawater only, seawater with 300–150 μm of SiC and seawater + 600–300 μm of SiC. The maps have been clearly drawn for three different speeds, and they are, respectively, indicated as (a) 2.5 ms^{-1}, (b) 4.5 ms^{-1} and (c) 6.5 ms^{-1}. Figure 19a indicates the rig has been operated, and the sample materials were eroded under 2.5 ms^{-1} at three different conditions. It clearly indicates the presence of medium wear, and it occurs at 45°–60°, and the seawater + two different test slurries share the boundary. The dominance of very low/mass gain wear can also be seen under the seawater condition, and the wear rate increases as the impact velocity increases. A very different behaviour is now observed, and Fig. 19b shows the occurrence of medium wear in the seawater + 300–150 μm. Although it shares the boundary with seawater + 600–300 μm, it mainly occurs in the lower region, and it is due to the intermediate operating
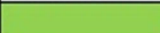
Boundary Limits	Grams	Color codes
Very low (15%)	0.000855	
Low (15–35%)	0.001995	
Medium (35–65%)	0.003705	
High (65–85%)	0.004845	
Severe (85–100%)	0.0057	

Fig. 18 Boundary limits with *colour codes* (Color figure online)

(a) 2.5ms⁻¹

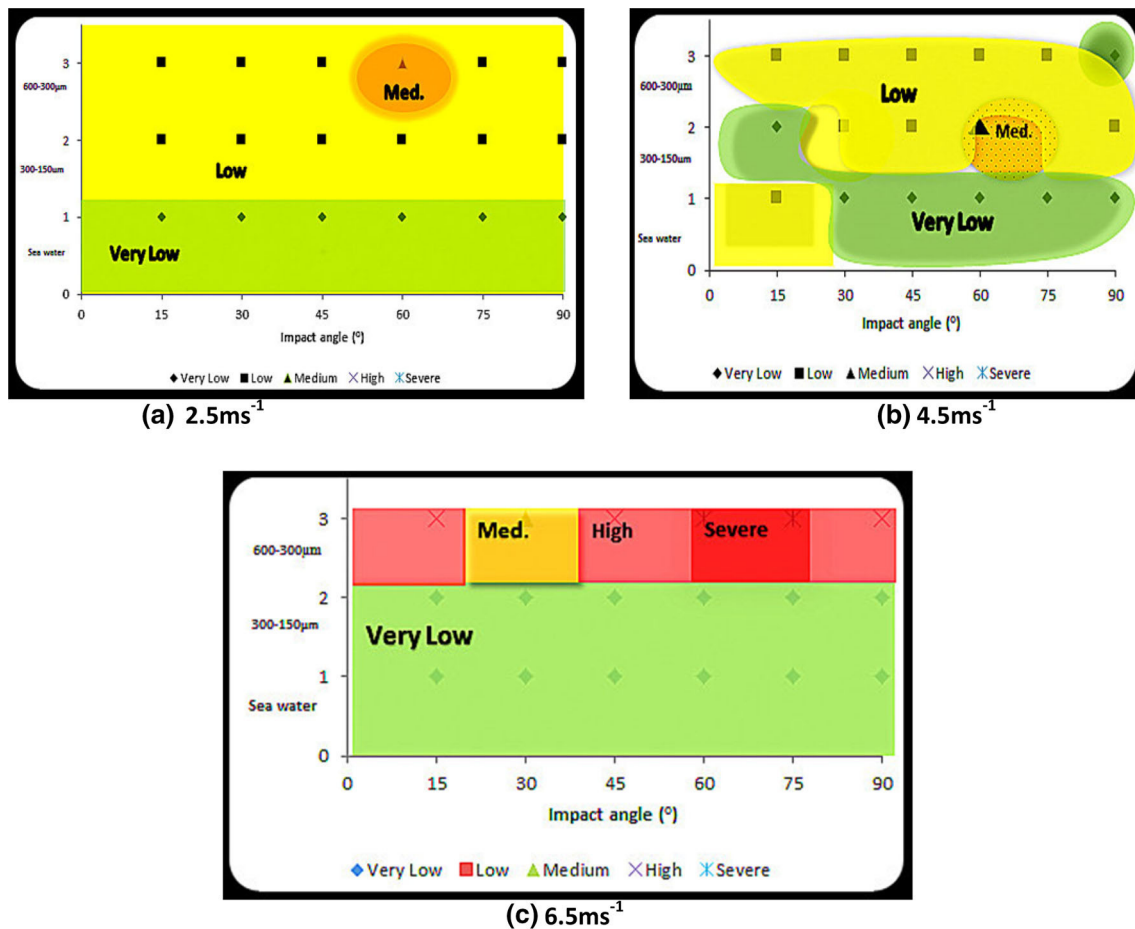**(b) 4.5ms⁻¹**

(c) 6.5ms⁻¹

Fig. 19 Wear mode map for three test conditions **a** 2.5 ms^{-1}, **b** 4.5 ms^{-1}, **c** 6.5 ms^{-1}

speed, which is 4.5 ms^{-1}, and it can be resolved by plotting error maps and also by surveying the comparative analysis between the error maps. As a result of comparison, there is almost no evidence indicating potential unsafe operating condition under seawater testing only for the limits set above, and for the experimental conditions evaluated in this study. Therefore, the combination of the very low/mass gain and low wear zones can be regarded as the safe operation zone for this material. Figure 19c shows the wear mode regimes for the maximum operating speed 6.5 ms^{-1}. A very different behaviour is now observed. It is clear from the map that very low wear dominates the wear mode regime, with severe wear being observed at intermediate impact angles and velocities. However, the medium and high wears occur at the low and high impact angles and velocities. This indicates that in the presence of particles, very significant increases in wear can be identified over such exposure conditions, limiting the performance of the material.

This wear mapping methodology for tidal turbine materials enables the optimum operating window to be identified for the exposure conditions and is a first step

approach towards developing smart materials for the exposure conditions. Further work will be to include additional factors such as different distributions of erodent particles, erosion exposure time and properties of the composite to understand the important factors which change the regime transitions above.

5 Concluding Remarks

(a) The combined influence of impingement angle and impact velocity on the erosive wear of the G.10-grade glass fibre-reinforced composite laminate resulted in semi-ductile erosive wear behaviour with a maximum wear at 60° impingement angle for the conditions studied.

(b) Wear mode maps were constructed to identify the minimum erosion zones in seawater conditions, with and without particles.

(c) SEM studies indicated that that erosion process for the composite was characterized by multiple cracks

coupled with cavity formation and multiple indentation sites associated with linear scratches.

(d) The combination of the aqueous environment containing salt together with solid particles amplified the erosion rate in a synergistic manner, thereby increasing the depth of penetration, leading in turn to extended crack propagation on the test samples.

(e) On-going work involves testing the sample materials under still water conditions and thereby bridging the gap between wear mode maps and constructing the unified mechanistic maps to identify the safe operating conditions.

References

1. Johnstone CM, Pratt D, Clarke JA, Grant AD (2013) A techno-economic analysis of tidal energy technology. Renew Energy 49:101–106

2. Tewari US, Harsha AP, Häger AM, Friedrich K (2003) Solid particle erosion of carbon fibre- and glass fibre-epoxy composites. Compos Sci Technol 63(3–4):549–557

3. Kim A, Kim I (2009) Solid particle erosion of CFRP composite with different laminate orientations. Wear 267(11):1922–1926

4. Bijwe J, Indumathi J, Johnrajesh J, Fahim M (2001) Friction and wear behavior of polyetherimide composites in various wear modes. Wear 249(8):715–726

5. Palin-Luc T, Pérez-Mora R, Bathias C, Domínguez G, Paris PC, Arana JL (2010) Fatigue crack initiation and growth on a steel in the very high cycle regime with sea water corrosion. Eng Fract Mech 77(11):1953–1962

6. Grewal HS, Singh H, Yoon E-S (2015) Interplay between erodent concentration and impingement angle for erosion in dilute water–sand flows. Wear 332–333:1111–1119

7. Arjula S, Harsha AP (2006) Study of erosion efficiency of polymers and polymer composites. Polym Test 25(2):188–196

8. Walker CI, Hambe M (2015) Influence of particle shape on slurry wear of white iron. Wear 332–333:1021–1027

9. Zu JB, Hutchings IM, Burstein GT (1990) Design of a slurry erosion test rig. Wear 140(2):331–344

10. S. Wedges, H. V. Insulation, T. Boards, T. Strips, T. Spacers, P. Barriers, E. C. Insulation, C. Components, C. R. Components, P. Insulation, I. B. Spacers, P. M. Parts, W. Absorption, and T. Index. G10 Product Data Sheet. vol. 44, no. 0, pp. 1–2

11. Stack MM, Abdulrahman GH (2012) Mapping erosion–corrosion of carbon steel in oil–water solutions: effects of velocity and applied potential. Wear 274–275:401–413

12. N. S. House and N. S. Avenue (1965) Commercial in confidence, no. November, pp. 1–41

13. Rattan R, Bijwe J (2007) Influence of impingement angle on solid particle erosion of carbon fabric reinforced polyetherimide composite. Wear 262(5–6):568–574

14. Wensink H, Elwenspoek MC (2002) A closer look at the ductile-brittle transition in solid particle erosion. Wear 253(9–10):1035–1043

15. Sparks AJ, Hutchings IM (1991) Transitions in the erosive wear behaviour of a glass ceramic. Wear 149(1–2):99–110

16. Hutchings I (1995) Friction and wear of ceramics. Tribol Int 28(6):421–422

17. Patnaik A, Satapathy A, Chand N, Barkoula NM, Biswas S (2010) Solid particle erosion wear characteristics of fiber and particulate filled polymer composites: a review. Wear 268(1):249–263

18. Patnaik A, Biswas S, Kaundal R, Satapathy A (2006) Damage assessment of short glass fiber reinforced polyester composites. InTechOpen, 2006

19. Momber AW (2014) Effects of target material properties on solid particle erosion of geomaterials at different impingement velocities. Wear 319(1–2):69–83

20. Grogan DM, Leen SB, Kennedy CR, Brádaigh CMÓ (2013) Design of composite tidal turbine blades. Renew Energy 57:151–162

21. Lim S (1998) Recent developments in wear-mechanism maps. Tribol Int 31(1–3):87–97

22. Stack MM (2005) Bridging the gap between tribology and corrosion: from wear maps to Pourbaix diagrams. Int Mater Rev 50(1):1–17